Contents lists available at SciVerse ScienceDirect

Nuclear Instruments and Methods in Physics Research A

journal homepage: www.elsevier.com/locate/nima

Analysis of the imaging performance in indirect digital mammography detectors by linear systems and signal detection models

P. Liaparinos *, N. Kalyvas, I. Kandarakis, D. Cavouras

Department of Medical Instruments Technology, Technological Educational Institute, 122 10 Athens, Greece

ABSTRACT

Purpose: The purpose of this study was to provide an analysis of imaging performance in digital mammography, using indirect detector instrumentation, by combining the Linear Cascaded Systems (LCS) theory and the Signal Detection Theory (SDT). Observer performance was assessed, by examining frequently employed detectors, consisting of phosphor-based X-ray converters (granular Gd_2O_2S:Tb and structural CsI:Tl), coupled with the recently introduced complementary metal-oxide-semiconductor (CMOS) sensor. By applying combinations of various irradiation conditions (filter-target and exposure levels at 28 kV) on imaging detectors, our study aimed to find the optimum system set-up for digital mammography. For this purpose, the signal to noise transfer properties of the medical imaging detectors were examined for breast carcinoma detectability.
Methods: An analytical model was applied to calculate X-ray interactions within software breast phantoms and detective media. Modeling involved: (a) three X-ray spectra used in digital mammography: 28 kV Mo/Mo (Mo: 0.030 mm), 28 kV Rh/Rh (Rh: 0.025 mm) and 28 kV W/Rh (Rh: 0.060 mm) at different entrance surface air kerma (ESAK) of 3 mGy and 5 mGy, (b) a 5 cm thick Perspex software phantom incorporating a small Ca lesion of varying size (0.1–1 cm), and (c) two 200 μm thick phosphor-based X-ray converters (Gd2O2S:Tb, CsI:Tl), coupled to a CMOS based detector of 22.5 μm pixel size.
Results: Best (lowest) contrast threshold (CT) values were obtained with the combination: (i) W/Rh target-filter, (ii) 5 mGy (ESAK), and (iii) CsI:Tl-CMOS detector. For lesion diameter 0.5 cm the CT was found improved, in comparison to other anode/filter combinations, approximately 42% than Rh/Rh and 55% than Mo/Mo, for small sized carcinoma (0.1 cm) and approximately 50% than Rh/Rh and 125% than Mo/Mo, for big sized carcinoma (1 cm), considering 5 mGy X-ray beam. By decreasing lesion diameter and thickness, a limiting CT (100%) was occurred for size values less than 0.2 cm.
Conclusion: CT was found to be affected by the selection of target/filter and exposure combination. It was found that the optimum thickness of CsI:Tl was approximately 190 μm and for Gd_2O_2S:Tb 120 μm for the studied energy and ESAK range.

1. Introduction

Image quality for medical purposes is related to the useful diagnostic information that can be extracted from an image. This quality can be evaluated by the performance of "some type of observer" on a particular diagnostic classification task [1,2]. The methodology used for human performance assessment can provide a relationship between objective image quality level and subjective diagnostic performance. In diagnostic medical imaging applications (i.e. X-ray mammography, chest radiography and X-ray computed tomography), where X-ray detectors are employed for image formation [3], an example of a classification task is the

lesion detection. X-ray detectors can play a critical role in improving image quality, since they can accurately acquire and depict spatial information carried by the X-ray beam transmitted through the patient.

In X-ray digital mammography, a very particular application of X-ray projection imaging, an attenuation profile of a human breast is projected onto a radiation detector often consisting of a phosphor-based X-ray converter, to convert X-ray energy to visible light photons. These photons are then captured by an electronic optical sensor. These converters are classified into two general categories: (a) indirect imaging detectors, using a granular phosphor screen (e.g., Gd_2O_2S:Tb) and (b) indirect imaging detectors, using a columnar phosphor screen (e.g., CsI:Tl) and exhibit advantages in several medical and industrial imaging applications [4]. Direct imaging detectors based on a-Se converting material are also currently employed in commercially available

* Corresponding author.
 E-mail address: liapkin@teiath.gr (P. Liaparinos).

mammographic medical imaging systems [5,6]. However, ongoing investigations are aimed at improving the gain of a-Se based detectors through avalanche multiplication process and in understanding its implication on noise [7]. A direct a-Se converter exhibits lower sensitivity [8] and in particular has been found at least half for 20 keV X-ray energy and phosphor thickness 50–100 mg/cm^2 [9] compared to the phosphor-based converters (e.g., Gd_2O_2S:Tb, CsI:Tl). Thus, the development of low-noise detectors with improved sensitivity would also be beneficial to the promising technique of digital breast tomosynthesis (DBT) that requires low dose per projection view [7]. A point worth commenting is that the two X-ray detective modalities have been configured with different X-ray beam spectra qualities (Mo/Mo, Mo/Rh, Rh/Rh for indirect detection and W/Rh, W/Ag for direct detection).

Image quality (i.e. contrast, resolution, noise and brightness) depends on the imaging performance (signal to noise ratio - SNR) of the X-ray converter, which in turn is directly affected by its intrinsic physical and structural properties [10,11]. Within the past years, the use of a model observer, which combines physical detector parameters, imaging conditions and object detectability tests, has been considered an attractive method to optimize detector imaging performance [12,13]. The development of model observer overcomes some of the limitations in using the overall signal to noise properties of the detector [14,15], expressed by the detective quantum efficiency (DQE) in the sense that they are applied in clinical X-ray irradiation and image observation conditions and accounts for the effect of human eye and medical doctor experience in detail resolving. Various investigations have utilized observer models for the assessment of medical image quality in imaging modalities [16–21]. In particular, two significant contributions [12,13] have performed studies on digital mammographic systems. Their results provided prediction of object detectability and led to further optimization of the imaging procedure [22].

However, the effects of observer models on the imaging performance of indirect phosphor-based X-ray detectors for carcinoma detectability purposes have not been previously systematically studied in digital mammography. In addition, this challenge would be more interesting by combining the phosphor material with recent high definition optical detectors [23]. Various optical sensors have been used in medical imaging (e.g., mammographic film, a-Si flat panel imagers AMFPI, charge-coupled devices CCD etc); however, recently complementary metal–oxide–semiconductor (CMOS) imaging detectors seem to provide many advantages such as low power consumption, low production cost, wide dynamic range and "system on chip" capabilities, the radiation detecting layer is simple to fabricate and can be made out of nonstandard semiconductors [24].

This paper was aimed to provide an analysis of conditions to investigate the imaging performance of indirect detectors for digital mammography. This analysis was based on models for: (i) objective quality metrics, in the framework of the LCS theory, and (ii) observer performance in Signal Detection Theory (SDT), i.e. SNR and contrast threshold (CT). The models were applied to assess the performance of two phosphor-based detector configurations irradiated by X-ray spectra currently employed in digital mammography. Model observers were described through theoretical analysis characterizing the overall imaging detector performance [18] (i.e. the modulation transfer function (MTF), the noise power spectra (NPS), and the DQE. This has been accomplished by employing a complete analytical model and taking into account the following: (a) three mammographic X-ray spectra: 28 kV Mo/ Mo (0.030 mm), 28 kV Rh/Rh (0.025 mm), 28 kV W/Rh (0.060 mm) and two entrance surface air kerma levels, 3 mGy and 5 mGy, (b) 5 cm thickness breast tissue equivalent phantom (perspex) incorporating a simulated lesion of varying diameter

(0.1–1 cm) and depth (height) and, (c) two currently and widely used phosphor materials (Gd_2O_2S:Tb, CsI:Tl) with thickness 200 μm, thickness value used in digital mammography, and (d) a CMOS Remote RadEye HR photodiode pixel array with a pixel pitch of 22.5 μm.

2. Materials and methods

2.1. General description of model

The geometry of the model is illustrated in Fig. 1. An X-ray beam was assumed to impinge on a phantom and then, after passing through the layer, to fall on the detector surface. The two areas of the phantom are thus projected on the detector surface. The energy of the X-ray photons was determined from an X-ray spectral distribution appropriate for applications in digital mammography. In particular, for the derivation of the spectral distribution [25], we considered X-ray spectra used in commercial medical imaging modalities, such as [26]: (i) Mo/Mo (filter thickness: 30 μm, (ii) Rh/Rh (filter thickness: 25 μm) and (iii) W/Rh (filter thickness: 60 μm), corresponding to 28 kV X-ray tube voltage and 3 mGy and 5 mGy entrance surface air kerma. The phantom was assumed to be a 5 cm thick breast tissue equivalent layer (Perspex) incorporating a simulated lesion (carcinoma) of varying diameter (0.1–1 cm). The reason to proceed with a single kVp was due to previous study [27], where it has been reported that the selection of found to have very little influence on image quality of different digital mammography systems and the limiting factor for the detection was noise rather than contrast. After beam attenuation through the phantom, our study utilized the LCS theory [15,28,29] to model the output of the detector. The LCS model was represented as a series of stages. Each stage (gain or blur) represents a
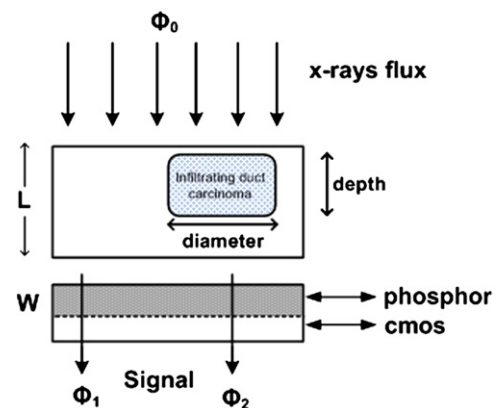
Fig. 1. Geometry of the model. Perspex phantom of 5 cm thickness consisting of two regions (the second part consists of a layer thickness separated to a thinner layer of the same material (Perpex) and another one of Carcinoma varying to several depths (0.1–1 cm). Carcinoma thickness was considered 0.5 cm.

Table 1
Physical and scintillating properties of granular Gd_2O_2S:Tb and columnar CsI:Tl phosphor materials: (i) material's density, ρ [9], (ii) packing density, ρ_p [14,54], (iii) intrinsic efficiency, η_c [14,15] and (iv) optical parameters σ, τ, ρ_0, ρ_1 (present study).

X-ray converter	Gd_2O_2S:Tb	CsI:Tl
Density ρ, (g/cm^3)	7.40	4.51
Packing density ρ_P	0.50	0.85
Intrinsic efficiency η_c	0.15	0.135
Reciprocal diffusion length σ, (cm^{2}g^{-1})	30	10
Inverse relaxation length, τ, (cm^{2}g^{-1})	222	1000
Back (input) reflection factor of the screen ρ_0	0.90	0.90
Front (output) reflection factor of the screen ρ_1	0.70	0.82

physical wide sense stationary (WSS) process that governs the transfer of signal from the input to the output [15,29]. In particular the detector was modeled as a system comprising a phosphor layer in contact with a CMOS pixel array optical sensor. In the phosphor layer, the local absorption of X-rays (without taking into account secondary X-ray interactions or scatter which is considerable small in the energy range used in mammography [11]), the production of light quanta and their corresponding escape to the output were taken into account. All the emerging light quanta were assumed to fall on the CMOS detector. However, due to spectral matching effects and the fill factor of the detector pixel, only a fraction was absorbed in the CMOS pixel to generate e–h pairs. The latter contribute, by a fraction, to the output signal [30]. The CMOS sensor was a Remote RadEye HR photodiode pixel array with a pixel pitch of 22.5 μm.

Two widely used phosphor materials were examined as X-ray converters: (a) the granular gadolinium oxysulphide ($Gd_2O_2S:Tb$) phosphor and (b) the columnar structured cesium iodide (CsI:Tl) phosphor. Advantages of $Gd_2O_2S:Tb$ are the X-ray detection properties, expressed by the Quantum Detection Efficiency (QDE), and the light emission efficiency (amount of light emitted per incoming or per absorbed amount of X-rays), i.e. the sensitivity
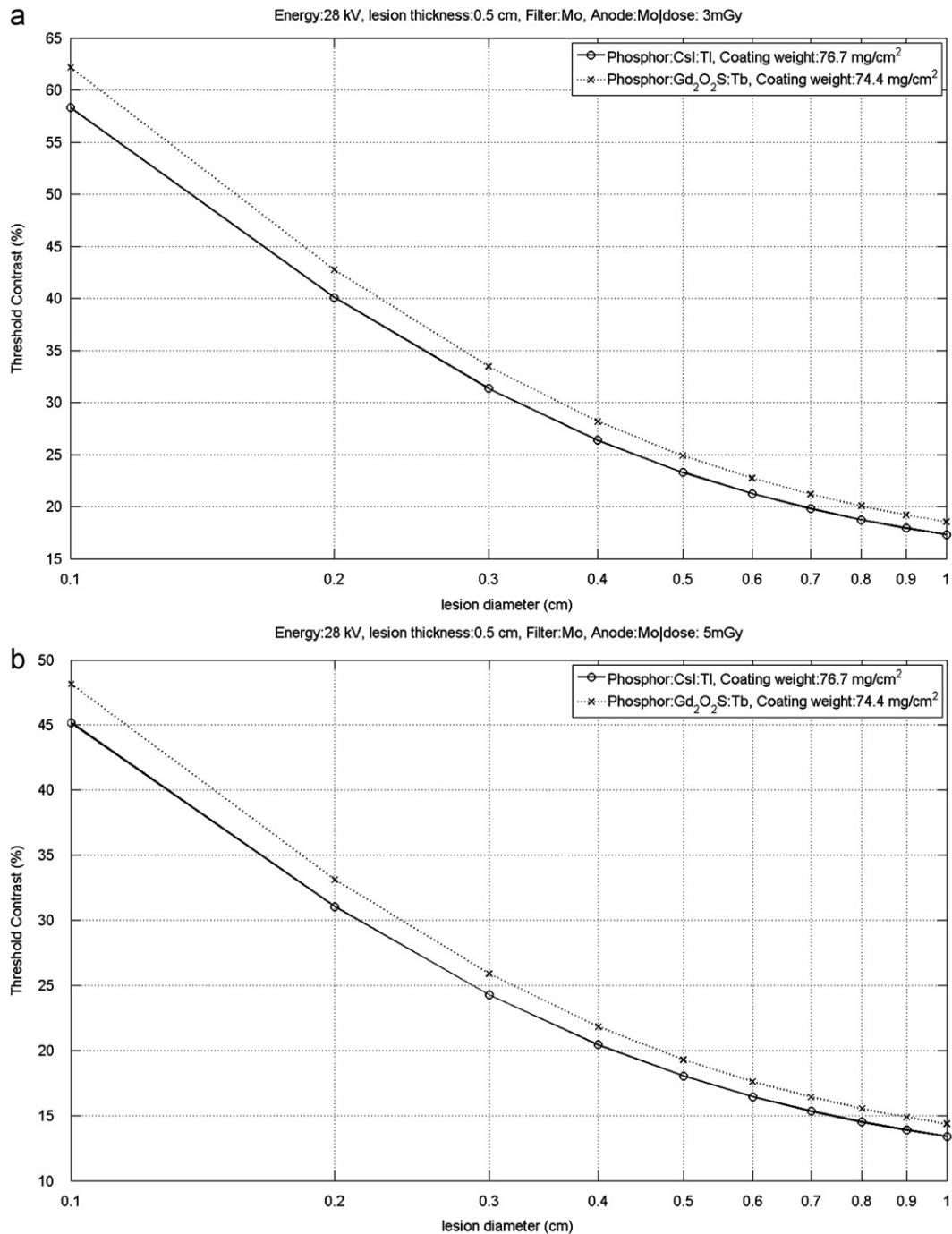
Fig. 2. Variation of CT as a function of carcinoma diameter (from 0.1 to 1 cm). Carcinoma thickness was considered 0.5 cm. Data are provided considering X-ray mammographic spectrum Mo/Mo (0.030 mm), X-ray tube voltage 28 kV, beam exposure (a) 3 mGy and (b) 5 mGy, irradiating 200 μm $Gd_2O_2S:Tb$ and CsI: Tl, phosphor layers coupled with CMOS detector array with pixel size 22.5 μm.

[31], which is also expressed by the number of light quanta emitted per absorbed X-ray [32] or the luminescence efficiency [33,34]. The higher detection efficiency of Gd_2O_2S:Tb is due to its high density (7.34 g/cm^3 for Gd_2O_2S:Tb and 4.51 g/cm^3 for CsI:Tl) and the high atomic number of the Gd element ($Z=64$), while its high amount of light emitted is mainly due to its high intrinsic efficiency [35,36]. On the other hand, CsI:Tl shows better signal transfer properties due to its columnar structure which reduces lateral light spread. This property provides an advantage for the development of high resolution detectors [4].

Data relevant to the X-ray attenuation coefficients of all materials used in our study (phantom and detector) were taken from validated data bases [37,38]. The set of the optical parameters (optical absorption and scattering coefficients) used for the granular (Gd_2O_2S:Tb) and the columnar (CsI:Tl) screens were estimated by model fitting based on reasonable agreement with published experimental MTF data [14,39]. For both phosphor screens, examined in this study a thickness of 200 μm was assumed. All intrinsic and physical properties used in the present model are given in Table 1.
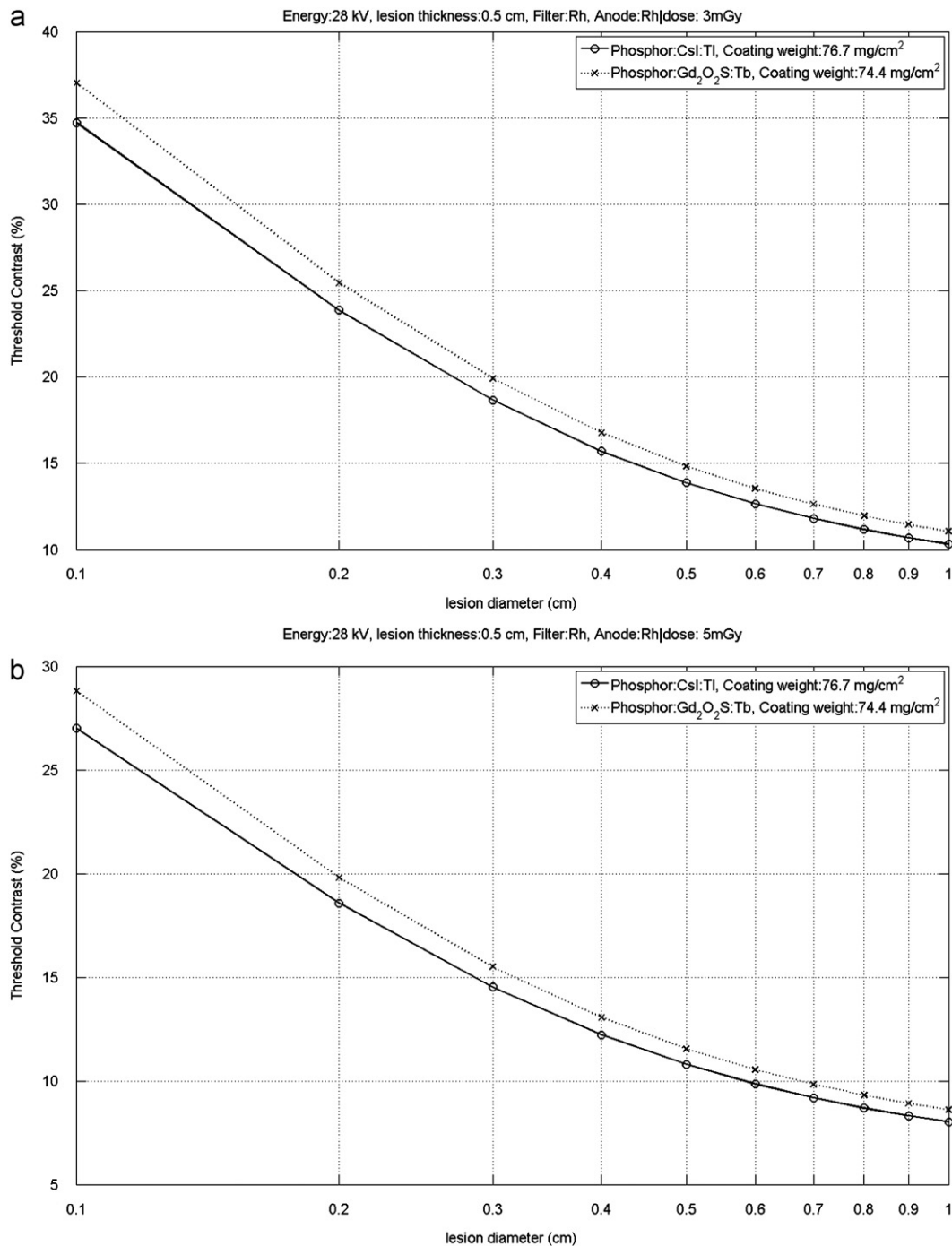
Fig. 3. Variation of CT as a function of carcinoma diameter (from 0.1 to 1 cm). Carcinoma thickness was considered 0.5 cm. Data are provided considering X-ray mammographic spectrum Rh/Rh (0.025 mm), X-ray tube voltage 28 kV, beam exposure (a) 3 mGy and (b) 5 mGy, irradiating 200 μm Gd_2O_2S:Tb and CsI: Tl, phosphor layers coupled with CMOS detector array with pixel size 22.5 μm.

## 2.2. Signal detection: SNR and CT evaluation in the framework of SDT

The SNR and the CT for the task of detecting a one dimensional object imaged against a homogeneous background can be given by the following expressions [12]:

$$SNR = \frac{C \int |S(u)MTF(u)O(u)|^2 \, du}{\int \left|S(u)MTF^2(u)O^2(u)\right|^2 \left(q_o DQE(u)^{-1} du\right)^{1/2}}. \qquad (1)$$

Table 2
MGD evaluations for three X-ray spectra (Mo/Mo, Rh/Rh, W/Rh) of different ESAK values (3 mGy and 5 mGy) irradiating 5 cm thickness breast tissue equivalent phantom (perspex).

X-ray spectrum	Incident ESAK MGD (mGy)	
	3 mGy	5 mGy
28 kV Mo/Mo (Mo: 0.030 mm)	0.54	0.90
28 kV Rh/Rh (Rh: 0.025 mm)	0.66	1.10
28 kV W/Rh (Rh: 0.060 mm)	0.92	1.54
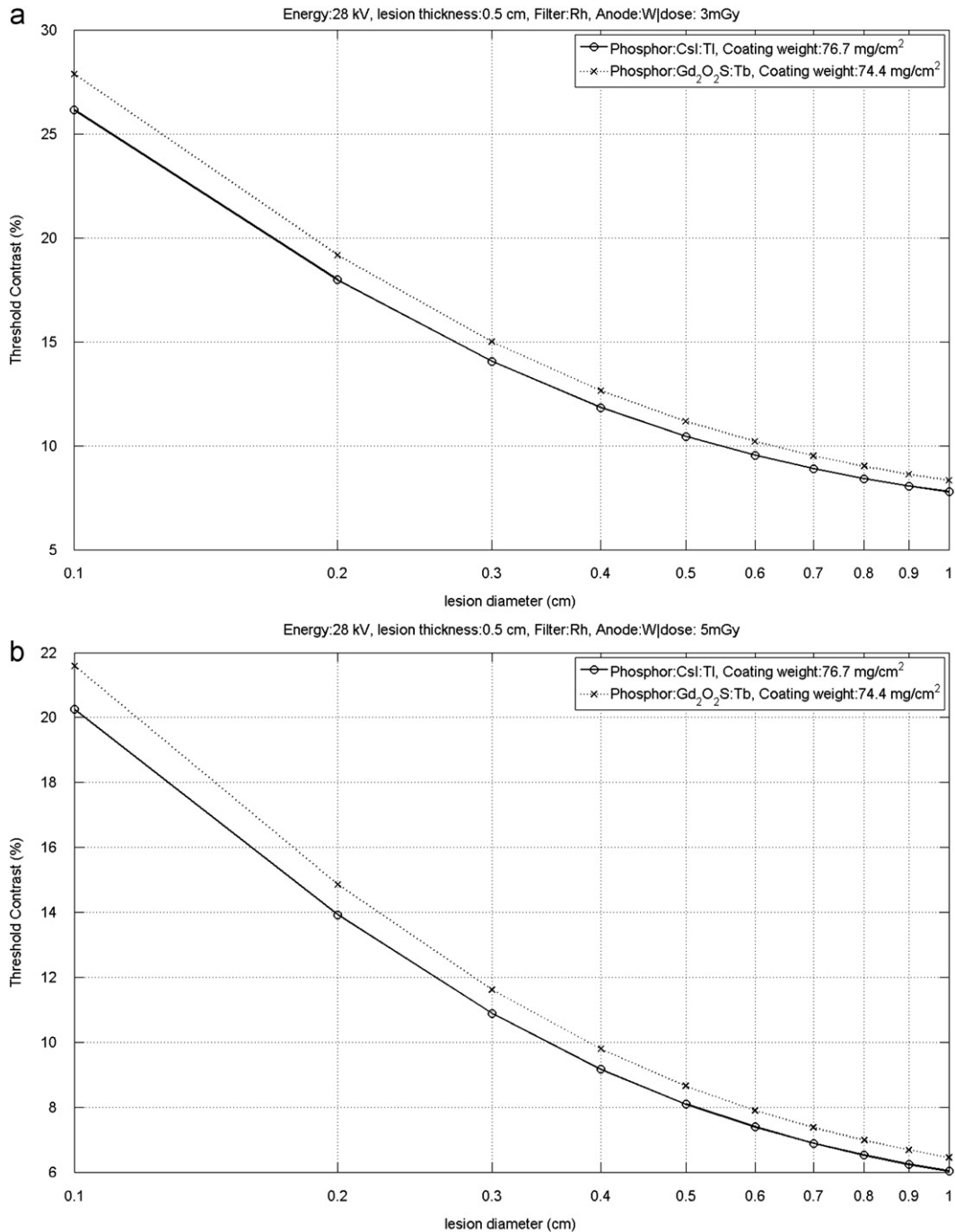
Fig. 4. Variation of CT as a function of carcinoma diameter (from 0.1 up to 1 cm). Carcinoma thickness was considered 0.5 cm. Data are provided considering X-ray mammographic spectrum W/Rh (0.060 mm), X-ray tube voltage 28 kV, beam exposure (a) 3 mGy and (b) 5 mGy, irradiating 200 μm Gd$_2$O$_2$S:Tb and CsI: Tl, phosphor layers coupled with CMOS detector array with pixel size 22.5 μm.

and

$$CT = k \left[\frac{C \int |S(u)MTF(u)O(u)|^2 du}{\int \left| S(u)MTF^2(u)O^2(u) \right|^2 \left(q_o DQE(u)^{-1} du \right)^{1/2}} \right]^{-1}. \tag{2}$$

where k is the observer's threshold SNR, which depends on the detection probability assumed by the observer. According to Eq. (2), as subject contrast increases an expected improvement of CT occurs. Regarding observer's threshold, high values of k correspond to well visualized objects only, shifts the calculated or expected threshold contrasts for the system with respect to the y-axis. On the other hand, a lower value for k corresponds to the capability of the observer in object detection even in poor imaging conditions. k was chosen to be 5 corresponding to strict observer demand [12]. $S(u)$ is the spectrum of the target object in frequency space. In particular, for the purposes of our study, $S(u)$ is derived from the Fourier transform of the object shown in Fig. 1. The imaging characteristics $MTF(u)$ and $DQE(u)$ are the corresponding modulation transfer function and the detective quantum efficiency of the corresponding X-ray detectors used for signal detection as given in Appendix A. III, $O(u)$ represents the spatial frequency response function of the observer's visual system [13], q_o is the X-ray signal given [12] and C is the signal difference (i.e. contrast) between the Perspex and the lesion corresponding to the two areas of the irradiated phantom projected on the detector surface (see section II.A). C can be calculated as follows:

$$C = \left| \frac{\int_E \phi_o(E)T_1(E) - \int_E \phi_o(E)T_1(E)}{\int_E \phi_o(E)} \right| \frac{1}{1 + (S/P)}. \tag{3}$$

where S/P is the scatter to primary ratio taken equal to 0.45 [12] and was assumed practical constant with respect to X-ray energy under consideration [40,41] and $\phi_o(E,T_i(E))$ is the X-ray photon fluence exiting the two regions of the phantom and $T_i(E)$, $i=1,2$ are the X-ray transmission functions expressing the attenuation of the X-ray beam penetrating the phantom as follows:

$$T_1(E) = \exp(-\mu_1(E)L). \tag{3a}$$

$$T_2(E) = \exp\left(-\int_i \mu_i(E)L_i \right). \tag{3b}$$

where E is the X-ray photon energy, L is the total thickness, of both parts, of the phantom.

3. Results and Discussion

3.1. Contrast threshold (CT)

The variation of CT as a function of carcinoma diameter is illustrated in Figs. 2–4 considering three X-ray mammographic spectra, respectively: Mo/Mo (0.030 mm), Rh/Rh (0.025 mm), and W/Rh (0.060 mm), at 28 kV. Two different ESAK cases were considered, 3 mGy and 5 mGy, both irradiating Gd_2O_2S:Tb and CsI:Tl phosphor-based detectors. The corresponding Mean Glandular Dose (MGD) for the aforementioned irradiation conditions are given in Table 2 and calculated as shown in Appendix B. Curves shown in Figs. 2–4 are provided for carcinoma depth 0.5 cm, phosphor thickness 200 μm, and CMOS pixel size 22.5 μm. Comparing different cases of X-ray spectrum, beam exposure and converter composition with the variation of object diameter (from 0.1 to 1 cm), results showed that the CT takes lower values for the case of W/Rh X-ray spectrum of 5 mGy irradiating the CsI:Tl/CMOS detector. In particular, for a small sized carcinoma of 0.1 cm in diameter, CT results are provided in Table 3. On the other hand, the detectability of large sized carcinomas (e.g., 1 cm)

Table 3
CT values (%) for three X-ray spectra (Mo/Mo, Rh/Rh, W/Rh) of different ESAK values (3 mGy and 5 mGy) irradiating 200 μm Gd_2O_2S:Tb and CsI: Tl, phosphor layers coupled with CMOS detector array of pixel size 22.5 μm. Carcinoma thickness was considered 0.1 cm.

Carcinoma size (0.1 cm)	X-ray converters					
	Gd_2O_2S:Tb			CsI:Tl		
	X-ray spectrum					
	Mo/Mo	Rh/Rh	W/Rh	Mo/Mo	Rh/Rh	W/Rh
ESAK (mGy)			CT (%)			
3	62.4	37.0	27.5	58.0	34.8	21.7
5	47.8	29.0	26.1	45.0	26.0	20.3

Table 4
CT values (%) for three X-ray spectra (Mo/Mo, Rh/Rh, W/Rh) of different ESAK values (3 mGy and 5 mGy) irradiating 200 μm Gd_2O_2S:Tb and CsI: Tl, phosphor layers coupled with CMOS detector array of pixel size 22.5 μm. Carcinoma thickness was considered 1 cm.

| Carcinoma size (1 cm)	X-ray converters					
	Gd_2O_2S:Tb			CsI:Tl		
	X-ray spectrum					
	Mo/Mo	Rh/Rh	W/Rh	Mo/Mo	Rh/Rh	W/Rh
ESAK (mGy)			CT (%)			
3	18.2	11.6	8.7	17.4	10.9	8.0
5	14.5	9.4	6.5	13.0	8.7	5.8

was found considerably improved than that of small sized carcinomas (e.g., 0.1 cm) as provided in Table 4. A point worth commenting is that our detector modeling does not take into account the effect of an antiscatter grid, since scattering contributes differently depending on the input spectrum for a 5 cm phantom [27]. In addition, CT results for each target/filter combination should always be assessed with respect to MGD. A more detailed analysis about spectra optimization can be found in the literature [42].

3.2. The effect of model parameters on CT

According to relation (2), the CT of carcinoma is expected to depend on the X-ray converter properties, mainly the MTF and DQE. Concerning the MTF, shown in Fig. 5(a), nearly identical MTF curves were obtained for all spectra considered in the present study, i.e. W/Rh, Rh/Rh, Mo/Mo at 5 mGy. Although, for a particular phosphor screen (composition and thickness) the MTF is expected to depend on the depth distribution of the absorbed X-ray energy, which in turn is affected by the shape of the X-ray spectrum, no significant effect of X-ray photon energy was observed on the MTF curves. This was due to: (i) the relatively small variations in the average energy of X-rays, among the various anode/filter combinations, which do not cause crucial modifications in the depth distribution of energy due to the absence of scattering and K X-rays, and (ii) the significance of light directivity (limited light spread) in columnar CsI:Tl phosphors, which compensates for depth effects and, thus, minimizes the corresponding depth dependent light spread. Similar results have been provided for different anode tube materials (Mo,W), but on a-Se based imaging detector [43].

Regarding, the effect of the X-ray energy (i.e. anode/filter combination) on DQE, it may be significant since this parameter depends directly on the X-ray absorption properties of phosphor,
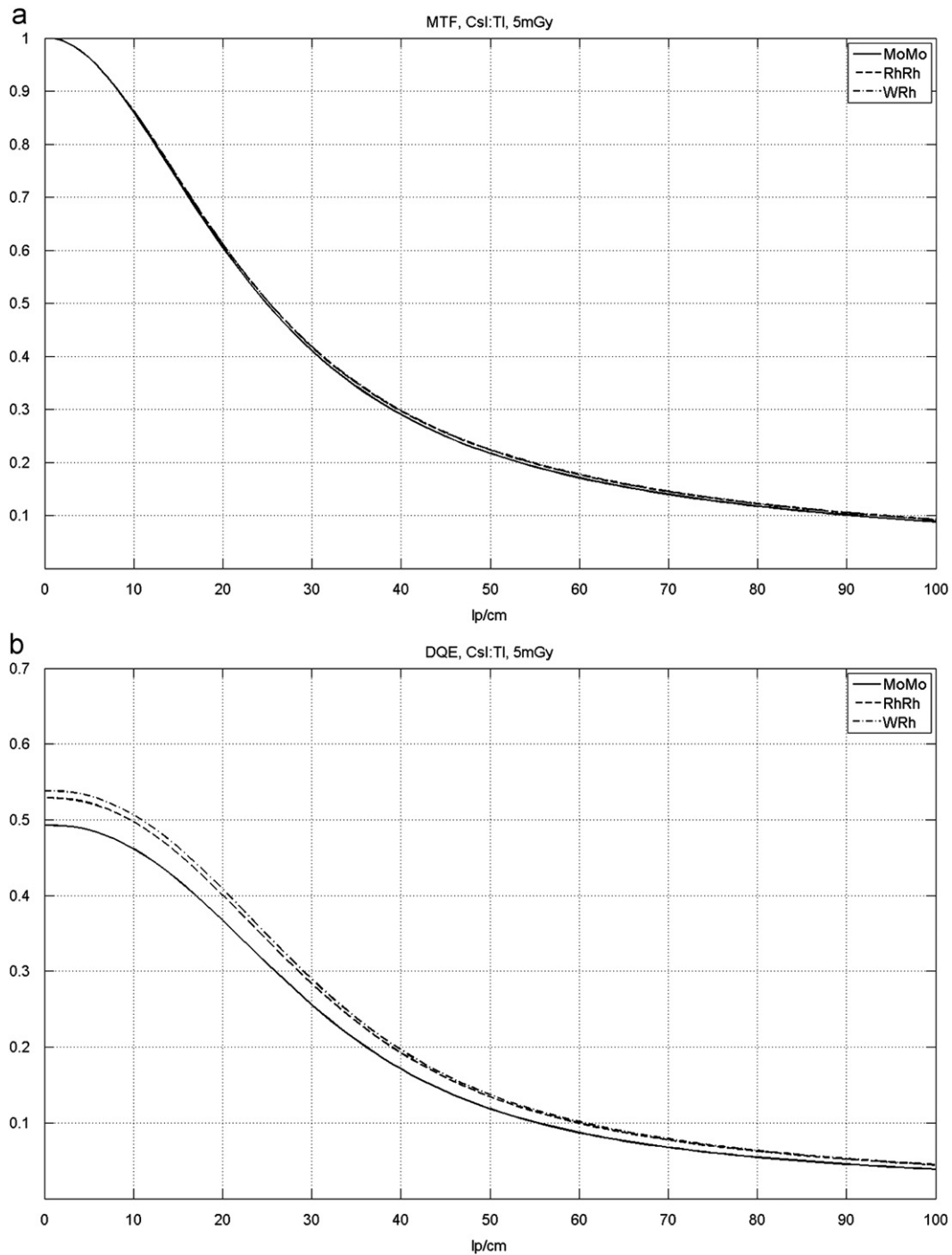
Fig. 5. Variation of MTF (a) and DQE (b) as a function of spatial frequency using beam exposure 5 mGy irradiating 200 μm CsI:Tl phosphor layer coupled with CMOS detector array of pixel size 22.5 μm. Data are provided for the X-ray spectra considered in our study: Mo/Mo, Rh/Rh and W/Rh.

expressed by the QDE. However, for the phosphor screen thickness assumed in the present study, no significant differences were found between the three anode/filter combinations: QDE= 0.887 (Mo,Mo), QDE=0.890 (RhRh) QDE=0.896 (WRh). As shown in the Fig. 5(b), the DQE corresponding to the W/Rh combination is slightly higher than that of the Rh/Rh combination and approximately 10% higher than that of the Mo/Mo combination (e.g., the zero-frequency DQE is approximately 0.54 for W/Rh and higher than 0.53 for Rh/Rh and 0.49 Mo/Mo). These differences in zero-frequency DQE values could be attributed to effects related to the statistical distribution of the optical pulses, created within the phosphor material, which are often expressed by the Swank

factor (SF). The W/Rh X-ray spectrum releases photons of slightly higher X-ray mean energy, which penetrates in depth more close to the rear surface of the converter. This causes a reduction in the number of light photon interaction events before escape. Thus, the fluctuations in amplitudes of light pulses decrease as compared to the other anode/filter combinations, resulting in increase on the detector's SNR, i.e., on SF and on zero-frequency DQE as well. At higher frequencies, the three curves of the frequency dependent DQE seem to coincide gradually (see Fig. 5b), since the influence of the MTF variation, which is practically identical for all anode/filter combinations, is more important at higher frequencies.
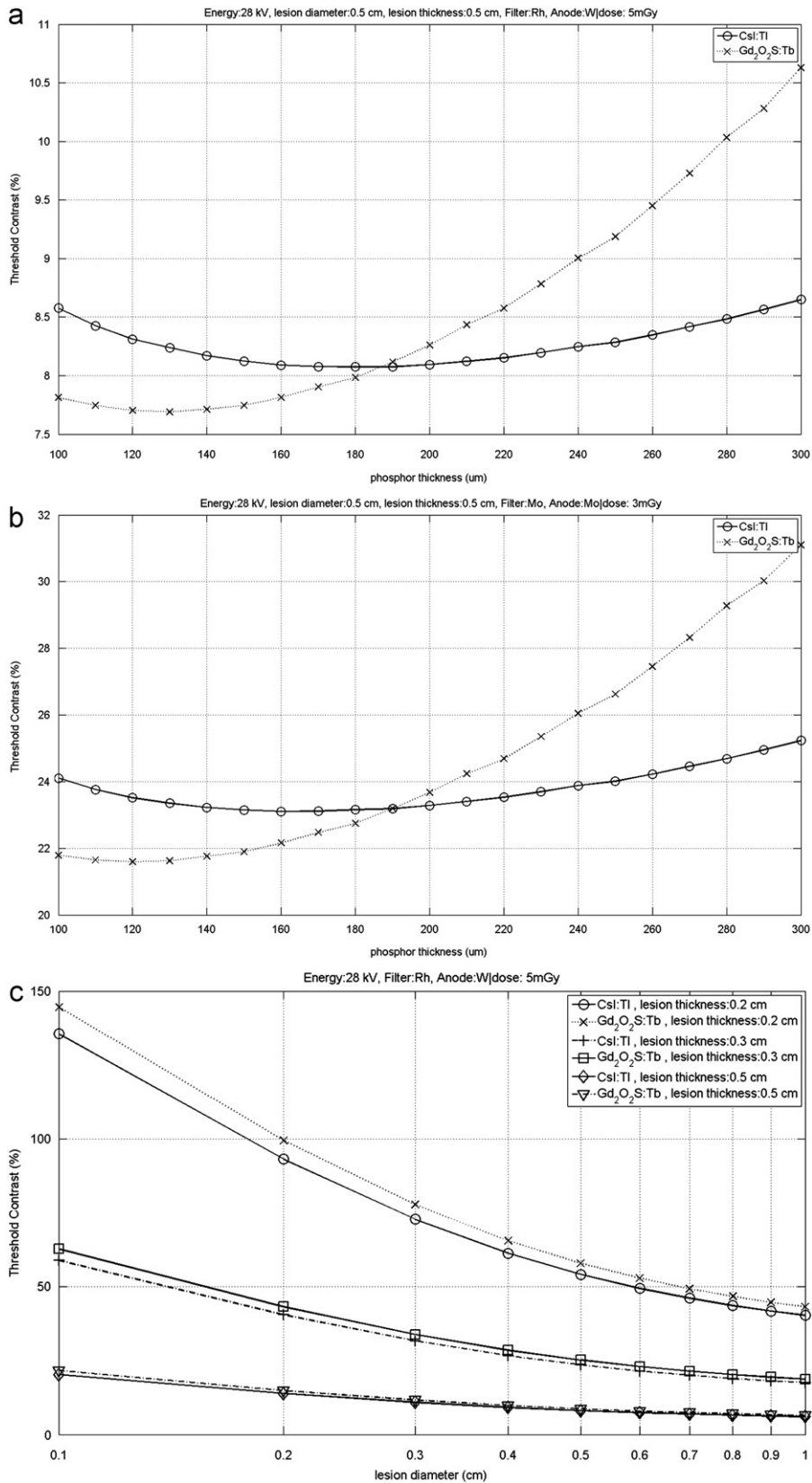
Fig. 6. (a) Variation of CT as a function of converter thickness diameter (from 100 to 300 μm). Carcinoma thickness was considered 0.5 cm. Data are provided considering X-ray mammographic spectrum W/Rh (0.060 mm), X-ray tube voltage 28kV, beam exposure 5 mGy, (b) Variation of CT as a function of converter thickness diameter (from 100 to 300 μm). Carcinoma thickness was considered 0.5 cm. Data are provided considering X-ray mammographic spectrum Mo/Mo (0.030 mm), X-ray tube voltage 28 kV, beam exposure 3 mGy, (c) Variation of CT as a function of carcinoma diameter (from 0.1 to 1 cm). Carcinoma thickness was considered 0.2, 0.3 and 0.5 cm. Data are provided considering X-ray mammographic spectrum W/Rh (0.060 mm), X-ray tube voltage 28 kV, beam exposure 5 mGy, irradiating 200 μm $Gd_2O_2S:Tb$ and CsI: Tl, phosphor layers coupled with CMOS detector array with pixel size 22.5 μm.

Under similar exposure conditions, a significant factor that seems to affect the threshold for the object detectability is the number of photons (q_0) incident on the converter [12]. This number is significantly higher for W/Rh, than Mo/Mo and Rh/Rh. This factor is also crucial comparing different exposure conditions for CT improvement at higher exposures (e.g., 5 mGy). The high value of q_0 in the case of W/Rh, is due to the beam hardness, since the mean energy of the X-ray photons is 19.3 keV, which is higher compared to the Mo/Mo (16.6 keV) and Rh/Rh (18 keV) X-ray spectra. A point worth commenting is that, recently, in digital mammography, the W/Rh spectrum has been adopted in commercial systems, which employ a-Se direct converters, instead of the traditional Mo/Mo spectrum. A combination of higher kVp and thicker converters has been also suggested [7,44,45].

In addition, the columnar structure of CsI:Tl converter limits the lateral spread of light and this property allows a CsI:Tl layer to be made thicker than a Gd_2O_2S:Tb layer for the same amount of spatial spread of the signal. The increased thickness allows greater X-ray absorption so that detectors consisting of CsI:Tl phosphor generally show equivalent imaging performance at lower X-ray exposure levels than Gd_2O_2S-based detectors [4]. Under similar X-ray exposure levels CsI:Tl phosphor becomes much more dominant. Figs. 6(a, b)
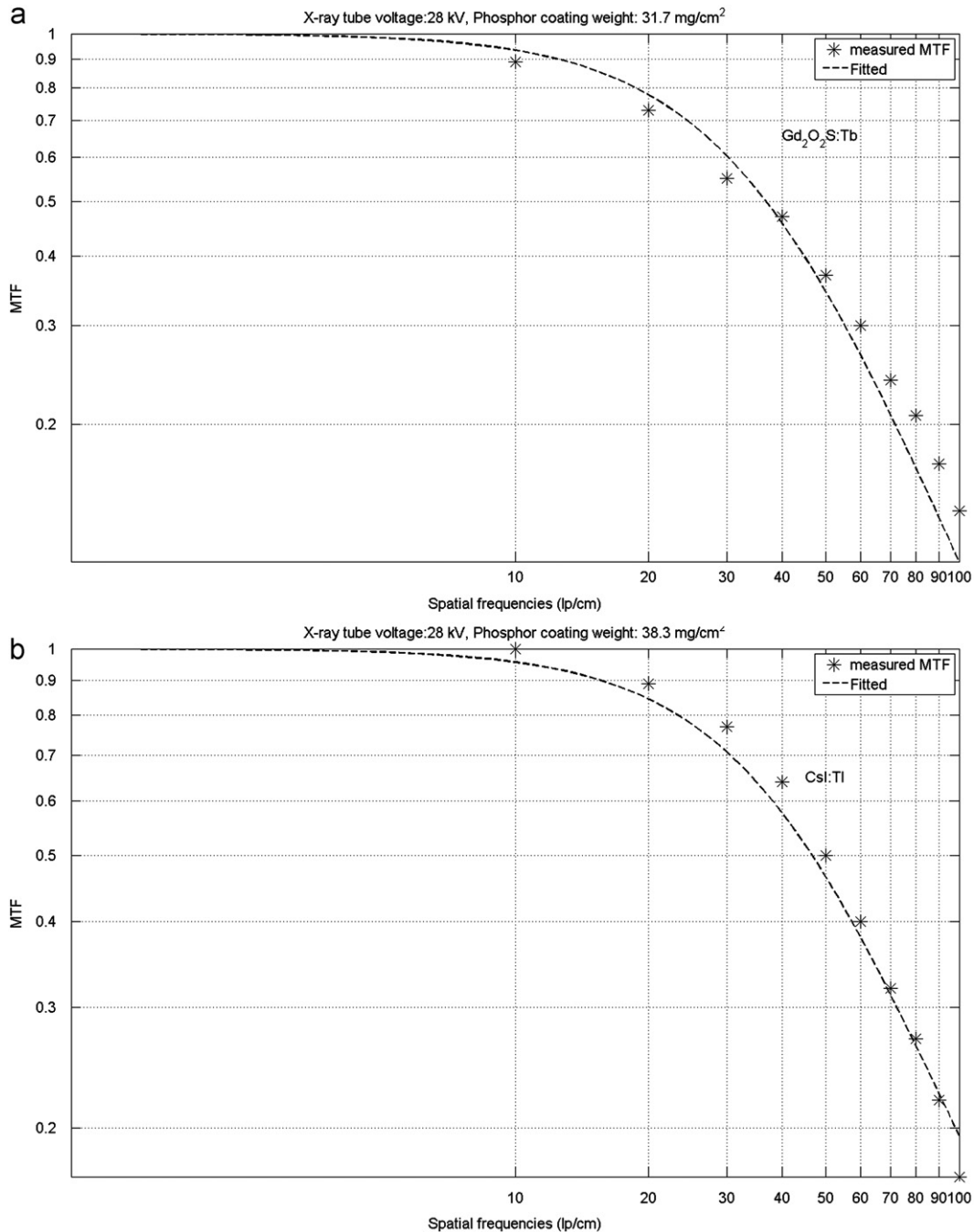
Fig. 7. Figure illustrates the variation of MTF as a function of spatial frequency. Lines correspond to the MTF fitting of the theoretical model and dots correspond to experimental data taken from the literature [14,39]. Figure (a) is referred to 31.7 mg/cm^2 Gd_2O_2S:Tb phosphor layer [14] and figure (b) to a 38.3 mg/cm^2 CsI:Tl phosphor layer [39].

illustrate CT values as a function of converter thickness (from 100 μm to 300 μm), for exposure conditions (Fig. 6a: 28 kV W/Rh, ESAK: 5 mGy, Fig. 6b: 28 kV Mo/Mo, ESAK: 3 mGy). In both cases, CT values of CsI:Tl are improved compared to Gd_2O_2S:Tb converter after a critical value of thickness (approximately 190 μm) presenting a highest difference at 300 μm (e.g., CT: 8.7% for CsI:Tl and 10.6% for Gd_2O_2S:Tb as shown Fig. 6a) due to the unique properties of high spatial resolution combined with thicker layers. In addition, the optimum thickness of Gd_2O_2S:Tb was found approximately at 120 μm which might provide an advantage of Gd_2O_2S:Tb in lower thickness values. Finally, by decreasing lesion diameter (from 1 cm to 0.1 cm) and thickness (from 0.5 cm to 0.2 cm), a limiting CT (100%) occurred for size values less than 0.2 cm (diameter and thickness), as shown in Fig. 6(c).

It may be of significance to note that the accuracy of our results is subject to limitations related to: (a) the model's dependence on tabulated physical data (Table 1), (b) analytical calculations based on diffusion light transfer theory; different values of optical parameters may affect considerably the plausibility of the results compared to experimental measurements, and (c) the effect of secondary particle (e.g., electrons) within the phosphor was not taken into account.

4. Conclusion

This paper presents an analysis of the imaging performance in indirect phosphor-based digital mammography converters coupled with CMOS detector array, by taking into account X-ray spectrum shape and fluence, X-ray detector properties, as well as signal detectability. The present study investigated the influence of X-ray spectra (anode/filter combinations, X-ray exposures) and converter composition of CT for carcinoma detectability at various lesion sizes. According to our findings, CT was found to be affected by the selection of target/filter and exposure combination. It was found that the optimum thickness of CsI:Tl was approximately 190 μm and for Gd_2O_2S:Tb 120 μm for the studied energy and ESAK range.

APPENDIX A:. Modeling the transfer of signal in the detector by LCS theory

A.I. Transfer of signal within the X-ray converter

The transfer of signal and noise in phosphor detectors in the frame of LCS has been studied in literature [14,15,29,30,46,47]. In this work we adopt the work of Nishikawa and Yaffe [14]. In this work the output noise and signal from the phosphor detector is given from the following equations:

$$NPS(u,W_o) = \int_E \int_w \overline{\phi}_o(E,T_2(E))\overline{n}_Q(E,W_o)\overline{\phi}_x(E,w)$$
$$\times \left[\overline{m}_o(E)\overline{G(w)MTF}(u,w)\right]^2 dwdE \quad (4)$$

and the mean number of light quanta exiting the phosphor equals to:

$$\overline{\Phi}_L(0,W_o) = \int_E \int_w \overline{\phi}_o(E,T_2(E))\overline{n}_Q(E,W_o)\overline{\phi}_x(E,w)\overline{m_o}$$
$$\times(E)\overline{G(w)MTF}(0,w)dwdE. \quad (5)$$

where $\overline{MTF}(0,w) = 1$.

Let us assume Poisson distributed number of photons $\overline{\phi}_o(E,T_2(E))$ is the number of photons incident on an elementary area of the detector. $\overline{n}_Q(E,Wo)$ is the fraction of $\phi_o(E,T_2(E))$ that will be absorbed in the phosphor, where Wo is the phosphor coating thickness, $\overline{\phi}_X(E,w)$ is the probability of X-ray absorption in each depth of elementary surface density dw, at a position between w and $w+dw$. $\overline{m}_o(E)$ is the mean number of optical photons that are produced per absorbed X-ray of energy E. $\overline{m}_o(E)$ is a function of the intrinsic conversion efficiency of the phosphor, n_C and the optical photon energy [14]. $\overline{G}(w)$ is the mean fraction of the optical quanta generated at w, which escape and spread to the output [14,17]. The total MTF of the phosphor screen of surface density Wo denoted as $\overline{MTF}_{scr}(u,Wo)$ can be calculated as $\overline{MTF}_{scr}(u,Wo) = \overline{\Phi}_L(u,Wo)/\overline{\Phi}_L(u,Wo)$, where, the values of $\overline{\Phi}_L(u,Wo)$ can be obtained if in Eq. (5), $\overline{G(w)MTF}(0,w)$ is substituted by the equations calculated needed for the calculation of $\overline{n}_Q(E,Wo)$, $\overline{m}_o(E)$ and $\overline{G(w)MTF}(u,w)$ can be found in previously published work [14,30,34]. A point worth commenting is that $\overline{G(w)MTF}(u,w)$ is a function of the phosphor optical properties reciprocal diffusion length, σ, inverse relaxation length τ, and the optical parameters ρ_0, ρ_1 expressing the reflection of light at the front and the back screen surfaces. In this study values of σ, τ, ρ_0, ρ_1 were found by fitting experimental MTF data, as shown in Fig. 7 for both phosphors, Gd_2O_2S:Tb (Fig. 7a) and CsI:Tl (Fig. 7b), and provided in Table 1.

A.II. Transfer of signal within the CMOS sensor

The transfer of the signal within the CMOS sensor has been described in a previous work. In summary: the escaping light quanta will impinge on the CMOS pixel and a fraction of these quanta will be actually. This is assumed to be a binomial distribution with a mean probability $\overline{ff}$, where $\overline{ff}$ is the fill factor of the pixel. In addition, the active area, denoted as a_{pd}^2 where, $a_{pd}^2 = f\overline{f}a_{pix}^2$ and a_{pix} is the pixel pitch. Upon incidence of the optical photons on the CMOS pixel, they are subjected to a deterministic blur process due to the finite dimensions of the aperture [29,30], which is characterized by an $MTF_{pix}(u)$ corresponding to the sinc function, i.e. $MTF_{pix}(u) = \sin c(\pi a_{pd}u)$. Due to spectral matching effects, only a fraction of these optical photons, are captured by the CMOS photodiode. This is a gain stage assumed to follow a binomial distribution characterized by a mean probability $\overline{a_s}$. The optical photon energy absorbed by the CMOS detector produces electron–hole (e–h) pairs. This is a gain stage (assumed to follow a binomial distribution) characterized by a mean probability $\overline{Q_p}$. The electrons are actually drifted and spread to the pixel output. This is a stochastic blur stage, however due to the infinitesimal spread, this stage was not taken into account [30]. Only a fraction of the electrons produced will reach to the output and will be accounted for the output signal of the detector. This is a gain stage (assumed to follow a binomial distribution) characterized by a mean probability $\overline{Q_e}$ By applying the LCS theory in the aforementioned stages the NPS of the detector, thereafter referred to as NPS_{CMOS}, is written as:

$$NPS_{CMOS}(u) = (\overline{ff}\,\overline{a_s}\overline{Q_p}\,\overline{Q_e})^2(NPS(u)\left[MTF_{pix}(u)\right]^2$$
$$+ \overline{\Phi}_L(0,W_o)\overline{ff}\,\overline{a_s}\overline{Q_p}\,\overline{Q_e}(1-\overline{ff}\,\overline{a_s}\overline{Q_p}\,\overline{Q_e}). \quad (6)$$

A point worth mentioning is that the above model does not take into account charge sharing effects. These occur, when an X-ray photon interacting in the sensor material gives rise to photoelectrons. These photoelectrons loose energy by scattering processes giving the resulting charge cloud a lateral dimension of a few microns. If the lateral broadening of the charge is significant in comparison with the pixel pitch, the charge cloud might be collected by several neighboring pixels. This effect degrades spatial resolution and contrast. Charge sharing is affected by the energy of the absorbed X-ray in the Si, the pixel dimensions the pixel gap and the thickness of the photoreceptor [48–51]. In our case the electrons produced by the optical photons have energies compared to the energy gap of Si ($\sim$eV). The X-ray photons that might interact with the CMOS material are around 10% of the incident spectrum (QDE$\sim$90%). In addition the thickness of the photoreceptor is in the order of several micrometers. Therefore this effect is less important in our case than in counting detectors which utilize materials with higher atomic number than Si. However the study of this effect should be a part of a future work.

A.III. Detector output final signal and DQE

The total mean number of electrons ($\overline{X_e}$) reaching the output can be calculated as the product of the mean number of each gain stage, as follows [30]:

$$\overline{X_e} = \overline{\Phi}_L(0, W_o) \overline{ff} \, \overline{a_s} \overline{Q_p} \, \overline{Q_e}. \tag{7}$$

The total MTF of the detector, $MTF_o(u)$ was calculated as the product of the mean MTF of each individual blur stage [29,30]: $MTF_o(u) = MTF_{scr}(u, W_o) MTF_{pix}(u)$. The product $\overline{ff} \, \overline{a_s} \overline{Q_p} \, \overline{Q_e}$ can be obtained from CMOS RadEye data sheet. It equals 0.37 for Gd_2O_2S:Tb phosphor and 0.4 for CsI:Tl phosphor. In addition $\overline{a_s} = 0.95$, $\overline{ff} = 0.80$, $\overline{a_{pd}} = 20.12 \, \mu m$

The DQE can be finally calculated as [29,46]:

$$DQE(u) = \frac{\left(\overline{X_e} MTF_o(u)\right)^2}{NPS_{CMOS}(u) \int_E \phi_o(E, T_2(E))}. \tag{8}$$

APPENDIX B. Mean Glandular Dose (MGD) evaluation

In order to determine the mean glandular dose, the half value layer (HVL) of the utilized X-ray spectrum should be calculated. The corresponding exposure (X) was calculated by the incident X-ray spectrum per incident X-ray energy as:

$$X(E)_{in} = 1.83 \times 10^{-6} \Phi_0(E) E \left(\frac{\mu_{en}(E)}{\rho}\right)_{air}. \tag{9}$$

where $\Phi_0(E)$ is the photon fluence (photons/mm^2), E is the photon energy (keV) and $\mu_{en}(E)/\rho$ is the air mass energy absorption coefficient (cm^2/g). The derived value for $X(E)_{in}$ was theoretically filtered by an aluminum foil of thickness t_{Al} per X-ray energy bin as:

$$X(E)_{out} = 1.83 \times 10^{-6} \Phi_0(E) E \left(\frac{\mu_{en}(E)}{\rho}\right)_{air} e^{-\mu_{Al}(E) t_{Al}}. \tag{10}$$

where $\mu_{Al}(E)$ is the X-ray attenuation coefficient of Al for energy E [52]. The value of t_{Al} was allowed to vary until $\sum_{E_{min}}^{E_{max}} X(E)_{out} / \sum_{E_{min}}^{E_{max}} X(E)_{in} = \frac{1}{2}$. The corresponding value of t_{Al} was assumed to correspond to HVL. The calculated HVL values were: 28 kV Mo/Mo (Mo:0.030 mm) HVL=0.31, 28 kV Rh/Rh (Rh:0.025 mm) HVL= 0.36, 28 kV W/Rh (Rh:0.060 mm) HVL=0.54. The mean glandular dose MGD can be calculated as $D_G = c_{DG50,Ki,PMMA} \, s \, ESAK$, where the values of $c_{DG50,Ki,PMMA}$ and s can be found in Tables 8.5 and Table 8.6 (Ref 53 pgs 162–163). According to Table 8.5 the

50 mm "standard" breast can be simulated with 45mm PMMA phantom.

References

[1] H.H. Barrett, J. Yao, J.P. Rolland, K.J. Myers, Proceedings of the National Academy of Sciences 90 (1993) 9758.
[2] K.J. Myers, Handbook of Medical Imaging, in: J. Beutel, H.L. Kundel, R.L. Van Metter (Eds.), Part 2, Phychophysics, vol 1, SPIE, Bellingham, WA, 2000.
[3] C.W.E. van Eijk, Physics in Medicine and Biology 47 (2002) R85.
[4] P.R. Granfors, D. Albagli, Journal of the Society for Information Display 17 (2009) 535.
[5] D.G. Darambara, Nuclear Instruments and Methods in Physics Research Section A 569 (2006) 153.
[6] J. Yorkston, Nuclear Instruments and Methods in Physics Research Section A 580 (2007) 974.
[7] A. Karellas, S. Vedantham, Medical Physics **35** (2008) 4878.
[8] H.K. Kim, I.A. Cunningham, Z. Yin, G. Cho, International Journal of Precision Engineering and Manufacturing 9 (2008) 86.
[9] P. Liaparinos, I. Kandarakis, Medical Physics 38 (2011) 4440.
[10] P. Liaparinos, I. Kandarakis, Physics in Medicine and Biology 54 (2009) 859.
[11] P. Liaparinos, I. Kandarakis, Medical Physics 36 (2009) 1985.
[12] N.W. Marshall, Physics in Medicine and Biology 51 (2006) 2441.
[13] J.A. Segui, W. Zhao, Medical Physics 33 (2006) 3711.
[14] R. Nishikawa, M. Yaffe, Medical Physics 17 (1990) 894.
[15] L.E. Antonuk, K.W. Jee, Y. El-Mohri, M. Maolinbay, S. Naddif, X. Rong, Q. Zhao, J.H. Siewerdsen, Medical Physics 27 (2000) 289.
[16] W. Hillen Schiebel, T. Zaengel, Physics in Medicine and Biology 14 (1987) 744.
[17] A. Workman, A.R. Cowen, Physics in Medicine and Biology 38 (1993) 1789.
[18] R. Aufrichtig, P. Xue, Physics in Medicine and Biology 45 (2000) 2653.
[19] N.W. Marshall, Physics in Medicine and Biology 46 (2001) 1631.
[20] R.M. Gagne, J.S. Boswell, K.J. Myers, Medical Physics 30 (2003) 2180.
[21] S. Vedantham, A. Karellas, IEEE Transactions on Medical Imaging 29 (2010) 790.
[22] C. Gheti, A. Borini, O. Ortenzia, R. Rossi, P.L. Ordóñez, Medical Physics 35 (2008) 456.
[23] P. Magnan, Nuclear Instruments and Methods in Physics Research Section A 504 (2003) 199.
[24] S.M. Gruner, M.W. Tate, E.F. Eikenberry, Review of Scientific Instruments 73 (2002) 2816.
[25] J.M. Boone, T.R. Fewell, R.J. Jennings, Medical Physics 24 (1997) 1863.
[26] M. Varjonen, P. Strömmer, Lecture Notes in Computer Science 5116 (2008) 570.
[27] W.J.H. Veldkamp, M.A.O. Thijssen, N. Karssemeijer, Medical Physics 30 (2003) 1712.
[28] C.D. Arvanitis, S.E. Bohndiek, G. Royle, A. Blue, H.X. Liang, A. Clark, M. Prydderch, R. Turchetta, R. Speller, Medical Physics 34 (2007) 4612.
[29] Y. El-Mohri, L.E. Antonuk, Q. Zhao, Y. Wang, Y. Li, H. Du, A. Sawant, Medical Physics 34 (2007) 315.
[30] C.M. Michail, V.A. Spyropoulou, G.P. Fountos, N.I. Kalyvas, I.G. Valais, I.S. Kandarakis, G.S. Panayiotakis, IEEE Transactions on Nuclear Science NS58 (2011) 314.
[31] M.J. Yaffe, J.A. Rowlands, Physics in Medicine and Biology 42 (1997) 1.
[32] C.E. Dick, J.W. Motz, Medical Physics 8 (1981) 337.
[33] G. Blasse, Journal of Luminescence 60&61 (1994) 930.
[34] I. Kandarakis, D. Cavouras, G.S. Panayiotakis, C.D. Nomicos, Physics in Medicine and Biology 42 (1997) 1351.
[35] P.F. Liaparinos, I. Kandarakis, D. Cavouras, H. Delis, G. Panayiotakis, Medical Physics 33 (2006) 4502.
[36] P. Liaparinos, I. Kandarakis, D. Cavouras, H. Delis, G. Panayiotakis, Medical Physics 34 (2007) 1724.
[37] P.C. Johns, M.J. Yaffe, Physics in Medicine and Biology 32 (1987) 675.
[38] J.H. Hubbell, S.M. Seltzer, Tables of X-ray Mass Attenuation Coefficients and Mass Energy-Absorption Coefficients from 1 keV to 20 MeV for Elements $Z=1$ to 92 and 48 Additional Substances of Dosimetric Interest, Report No. NISTIR 5632, National Institute of Standards and Technology, Gaithersburg, MD, 1995.
[39] S. Vedantham, A. Karellas, S. Suryanarayanan, D. Albagli, S. Han, E.J. Tkaczyk, C.E. Landberg, B. Opsahl-Ong, P.R. Granfors, L. Levis, C.J. D'orsi, R.E. Hendrick, Medical Physics 27 (2000) 558.
[40] J.M. Boone, K.K. Lindfors, V.N. Cooper III, J.A. Seibert, Medical Physics 27 (2000) 2408.
[41] E. Salvagnini, H. Bsmans, L. Struelens, N.W. Marshall, Medical Physics 39 (2012) 3167.
[42] N.T. Ranger, J.Y. Lo, E. Samei, Medical Physics 37 (2010) 962.
[43] A.P. Smith Hologic - Selenia: Digital Mammography 2011. ⟨http://www.hologic.com/en/breast-imaging/digital-mammography/selenia/⟩.
[44] D.R. Dance, A. Thilander Klang, M. Sandborg, C.L. Skinner, I.A. Castellano Smith, G.Alm Carlsson, British Journal of Radiology 73 (2000) 1056.
[45] P. Bernhardt, T. Mertelmeier, M. Hoheisel, Medical Physics 33 (2006) 4337.
[46] M. Rabbani, R. Shaw, R. Van Metter, Journal of the Optical Society of America A 4 (1987) 895.
[47] R.K. Swank, Applied Optics 12 (1973) 1865.
[48] F. Krejci, J. Jakubek, M. Kroupa, V. Jurka, K. Hruska, Journal of Instrumentation 6 (2011) C12034.

[49] L. Tlustos, M. Campbell, E. Heijne, X. Llopart, IEEE Transactions on Nuclear Science NS51 (2004) 3006.

[50] J.C. Kim, S.E. Anderson, W. Kaye, F. Zhang, Y. Zhu, S.J. Kaye, Z. He, Nuclear Instruments and Methods in Physics Research Section A 654 (2011) 233.

[51] K. Mathieson, M.S. Passmore, P. Seller, M.L. Prydderch, V. O'Shea, R.L. Bates, K.M. Smith, M. Rahman, Nuclear Instruments and Methods in Physics Research Section A 487 (2002) 113.

[52] R. Nowotny XMuDat, Photon attenuation data on PC. IAEA-NDS-195 International Atomic Energy Agency, Vienna, Austria. 1998.

[53] IAEA Technical Reports Series No. 457, Dosimetry in Diagnostic Radiology: An International Code of Practice IAEA, Vienna 2007, STI/PUB/1294.

[54] A. Badano, R.M. Gagne, B.D. Gallas, R.J. Jennings, J.S. Boswell, K.J. Myers, Medical Physics 31 (2004) 3122.